AMERICAN SOCIETY FOR MICROBIOLOGY | Applied and Environmental Microbiology®

MICROBIAL ECOLOGY

Subgroup Characteristics of Marine Methane-Oxidizing ANME-2 Archaea and Their Syntrophic Partners as Revealed by Integrated Multimodal Analytical Microscopy

Shawn E. McGlynn,[a,b,g] Grayson L. Chadwick,[a] Ariel O'Neill,[a] Mason Mackey,[c] Andrea Thor,[c] Thomas J. Deerinck,[c] Mark H. Ellisman,[c,d,e,f] Victoria J. Orphan[a]

[a]Division of Geological and Planetary Sciences, California Institute of Technology, Pasadena, California, USA
[b]Biofunctional Catalyst Research Team, RIKEN Center for Sustainable Resource Science (CSRS), Wako, Saitama, Japan
[c]National Center of Microscopy and Imaging Research (NCMIR), Center for Research on Biological Systems, University of California, San Diego (UCSD), School of Medicine, La Jolla, California, USA
[d]Department of Neurosciences, UCSD, La Jolla, California, USA
[e]Salk Institute for Biological Sciences, La Jolla, California, USA
[f]HHMI Janelia Research Campus, Ashburn, Virginia, USA
[g]Earth-Life Science Institute, Tokyo Institute of Technology, Meguro, Tokyo, Japan

ABSTRACT Phylogenetically diverse environmental ANME archaea and sulfate-reducing bacteria cooperatively catalyze the anaerobic oxidation of methane oxidation (AOM) in multicelled consortia within methane seep environments. To better understand these cells and their symbiotic associations, we applied a suite of electron microscopy approaches, including correlative fluorescence *in situ* hybridization-electron microscopy (FISH-EM), transmission electron microscopy (TEM), and serial block face scanning electron microscopy (SBEM) three-dimensional (3D) reconstructions. FISH-EM of methane seep-derived consortia revealed phylogenetic variability in terms of cell morphology, ultrastructure, and storage granules. Representatives of the ANME-2b clade, but not other ANME-2 groups, contained polyphosphate-like granules, while some bacteria associated with ANME-2a/2c contained two distinct phases of iron mineral chains resembling magnetosomes. 3D segmentation of two ANME-2 consortium types revealed cellular volumes of ANME and their symbiotic partners that were larger than previous estimates based on light microscopy. Polyphosphate-like granule-containing ANME (tentatively termed ANME-2b) were larger than both ANME with no granules and partner bacteria. This cell type was observed with up to 4 granules per cell, and the volume of the cell was larger in proportion to the number of granules inside it, but the percentage of the cell occupied by these granules did not vary with granule number. These results illuminate distinctions between ANME-2 archaeal lineages and partnering bacterial populations that are apparently unified in their ability to perform anaerobic methane oxidation.

IMPORTANCE Methane oxidation in anaerobic environments can be accomplished by a number of archaeal groups, some of which live in syntrophic relationships with bacteria in structured consortia. Little is known of the distinguishing characteristics of these groups. Here, we applied imaging approaches to better understand the properties of these cells. We found unexpected morphological, structural, and volume variability of these uncultured groups by correlating fluorescence labeling of cells with electron microscopy observables.

KEYWORDS ANME, DIET, polyphosphate metabolism, anaerobic methane oxidation, electron microscopy, fluorescence image analysis, sulfate reduction, syntrophy, ultrastructure

Received 15 February 2018 **Accepted** 31 March 2018

Accepted manuscript posted online 6 April 2018

Citation McGlynn SE, Chadwick GL, O'Neill A, Mackey M, Thor A, Deerinck TJ, Ellisman MH, Orphan VJ. 2018. Subgroup characteristics of marine methane-oxidizing ANME-2 archaea and their syntrophic partners as revealed by integrated multimodal analytical microscopy. Appl Environ Microbiol 84:e00399-18. https://doi.org/10.1128/AEM.00399-18.

Editor Haruyuki Atomi, Kyoto University

Address correspondence to Shawn E. McGlynn, mcglynn@elsi.jp, or Victoria J. Orphan, vorphan@gps.caltech.edu.

The development of electron microscopy (EM) over 6 decades ago provided an unprecedented view into the fine structure, complex organization, and positioning of key molecular machinery within bacterial, archaeal, and eukaryotic cells and tissues of plants and animals. In the study of bacteria and archaea, the vast majority of EM investigations have been of cultured microorganisms. While genomic knowledge of microbial interactions and diversity in the environment has increased significantly in the past decade (for example, see references 1 and 2), there is a critical gap in our understanding of the structural and functional specializations within uncultivated microorganism. Ultrahigh-resolution observation of phylogenetically identified uncultured environmental microorganisms can offer unique insights. For example, recently discovered "hami" grappling hooks within the altiarchaea (3, 4), unique intracellular structures in "ARMAN" archaea (5), multicellular magnetotactic bacteria (6), and intracytoplasmic anammoxosome membrane-bounded organelles in *Planctomycetes* (7) have all revealed continued insights that are being derived from high-resolution microscopy studies of diverse microbes.

In this study, we applied correlative microscopy methods that directly couple 16S rRNA identification by fluorescence *in situ* hybridization (FISH) and transmission electron microscopy (TEM; collectively termed FISH-EM) on uncultured methanotrophic microbial consortia living in deep-sea methane seep sediments to study the ultrastructure of phylogenetically distinct methanotrophic ANME-2 archaeal subgroups (ANME-2b and ANME-2c) and their associated syntrophic sulfate-reducing bacterium (SRB) partners. To quantify the ultrastructural features and variation in ANME and SRB biovolumes within these consortia, we additionally developed protocols for serial block face scanning electron microscopy (SBEM). These cells together perform sulfate-coupled anaerobic oxidation of methane (AOM) (8–10), and molecular 16S rRNA surveys and FISH microscopy have shown these archaeal and bacterial groups are phylogenetically and morphologically diverse, forming structured, multicelled consortia, each comprised of one ANME and one bacterial group per microbial consortium, most commonly in conjunction with a sulfate-reducing member of the *Deltaproteobacteria* (see, for example, references 8, 11, and 12). While inquiry into the genomes of these organisms (13–19) and their physiology (20–26) continues to expand our knowledge, basic elements of cell physiology and ultrastructure remain to be determined. In particular, very little is known about physiological differentiation between the various phylogenetic groups thought to be involved in the AOM process.

RESULTS AND DISCUSSION

FISH-EM reveals ultrastructure variation between distinct clades of ANME-2 archaea and partnering *Deltaproteobacteria*. To target a broad diversity of ANME lineages and examine potential clade-specific variation in ultrastructural features, FISH probe combinations, including ANME-2 (ANME-2-538) (27) and a deltaproteobacterial (DELTA495a) (28) probe, were used. In separate experiments, more specific probes targeting ANME-2c (ANME-2c-760) (12), the seep1a group within the *Desulfobacteraceae* (seep1a-1441) (29), and ANME-2b (ANME-2b-729) (25, 30) were used (Table 1). The application of these probes with different specificities allowed for the assignment of ultrastructural features to specific ANME-2 lineages.

FISH-EM description of the ultrastructure of ANME-2b archaea and chemical characterization of intracellular storage granules. A previously developed FISH probe (25, 30) was utilized to investigate ANME-2b archaea by EM (Fig. 1). 16S rRNA sequences from this ANME-2 subgroup have been commonly recovered from methane seeps from Hydrate Ridge, OR; Eel River basin, CA; and Mound 12 in Costa Rica and at a methane hydrate site in the Nankai Trough, Japan (9, 33, 34).

Identified ANME-2b cells frequently occurred as *Methanosarcina*-like packets reminiscent of *Methanosarcina mazei* (35). A prominent ultrastructural feature of the FISH-identified ANME-2b was the occurrence of ~100-nm-diameter intracellular granules, frequently occurring as one granule per cell but observed with as many 4 per cell (see, for example, the inset in Fig. 1i and similar features in the other panels). These

TABLE 1 FISH probes and formamide percentage used in FISH-EM hybridization

Probe	% formamide in hybridization buffer	Reference(s)
ANME-2c-760, dual Cy3	60	12
DSS658, dual Cy5	60	31
ANME-2-538, dual Cy3	45	27
seep1a-1441, dual Cy5	45	29
ANME-2b-729, dual Cy3	35	25, 30
DELTA495a, dual Cy5	35	28, 32
cDELTA495a (competitor)	35	28

structures were observed in 16 of the 18 consortia analyzed by FISH-TEM. After FISH hybridization, these granules appeared to lose much of their electron-dense contents, likely due to incubation with detergents like Triton X-100 and the metal chelator EDTA; however, enough material remained for analysis by energy dispersive spectroscopy (EDS) to determine elemental composition. This analysis revealed that the electron contrasting material in the granule is likely polyphosphate, containing P with variable amounts of metal cations, including (in granules from cells in different consortia) Zn, Ca, Fe, occasionally Ba, and possibly Cu (Fig. 2 and 3). To confirm the chemical identification of the granules, we also analyzed morphologically similar consortia not subjected to the detergent- and EDTA-containing FISH hybridization protocol. These consortia were fixed with glutaraldehyde and appeared to better preserve the electron-dense granule content, although some granules still appeared empty after this treatment. Intact granules in these preparations were much darker (more electron beam impermeable) and produced enhanced EDS intensity, with clear P signal and iron, which presumably functions as a charge-balancing cation (Fig. 3). Similar results were observed for cells from both the 5133 incubation (Fig. 3) and 3730 (see Fig. S1 in the supplemental material). As information about the molecular configuration of the atoms is currently unknown, we conservatively refer to these granules as polyphosphate-like granules (pPLGs) in this study. The mechanism causing removal of the pPLG material is not known but could be a preparation artifact or be associated with the physiological state of the cell, where the cell has metabolized the polyphosphate material and retained the vacuole. Phosphorus granules in *Alphaproteobacteria* have also been observed in an empty state (36, 37), but the cause of these observations together warrants additional study.

The composition of the ANME-2b pPLG is similar to that of granules previously described in some methanogens, including members of the *Methanosarcinales* and *Methanospirillum hungatei* (38–40), and, to a lesser extent, to that of the smaller granules found in *Methanosarcina mazei* (41). The anionic phosphate within these granules has been shown to bind various cations, including those of Fe, Ca, Mg, and Cu, suggesting that these granules function as metal storage components in addition to a source of phosphate (38). Toso and others (40) studied granules in *M. hungatei* by cryo-EM and reported similar elemental composition, suggesting that the ability to produce these granules exists across diverse euryarchaeal methanogens and ANME. It is yet to be determined how these granules are synthesized in archaea, but some euryarchaea contain genes encoding proteins for polyphosphate kinase 1 and 2 (42); however, the vacuolar (VTC) system has yet to be identified in ANME or other archaea (43).

Since phosphate bonding in polyphosphate inclusions occurs through repeating phospho-anhydride units, they could represent a significant store of cellular energy. Assuming the molecular stoichiometry of polyphosphate, Toso and coworkers estimated the potential chemical energy available during hydrolysis of these granules based on volume and density and suggested that 13×10^{-5} pmol of ATP equivalents could be stored within them, approximately 100-fold more phospho-anydride bond energy than could be expected in the cytoplasm assuming a 2 mM intracellular concentration of ATP (40). This possible storage of energy by both methanogens and methanotrophs (ANME) warrants further investigation, as both physiologies are believed to persist in low-available-energy environments.

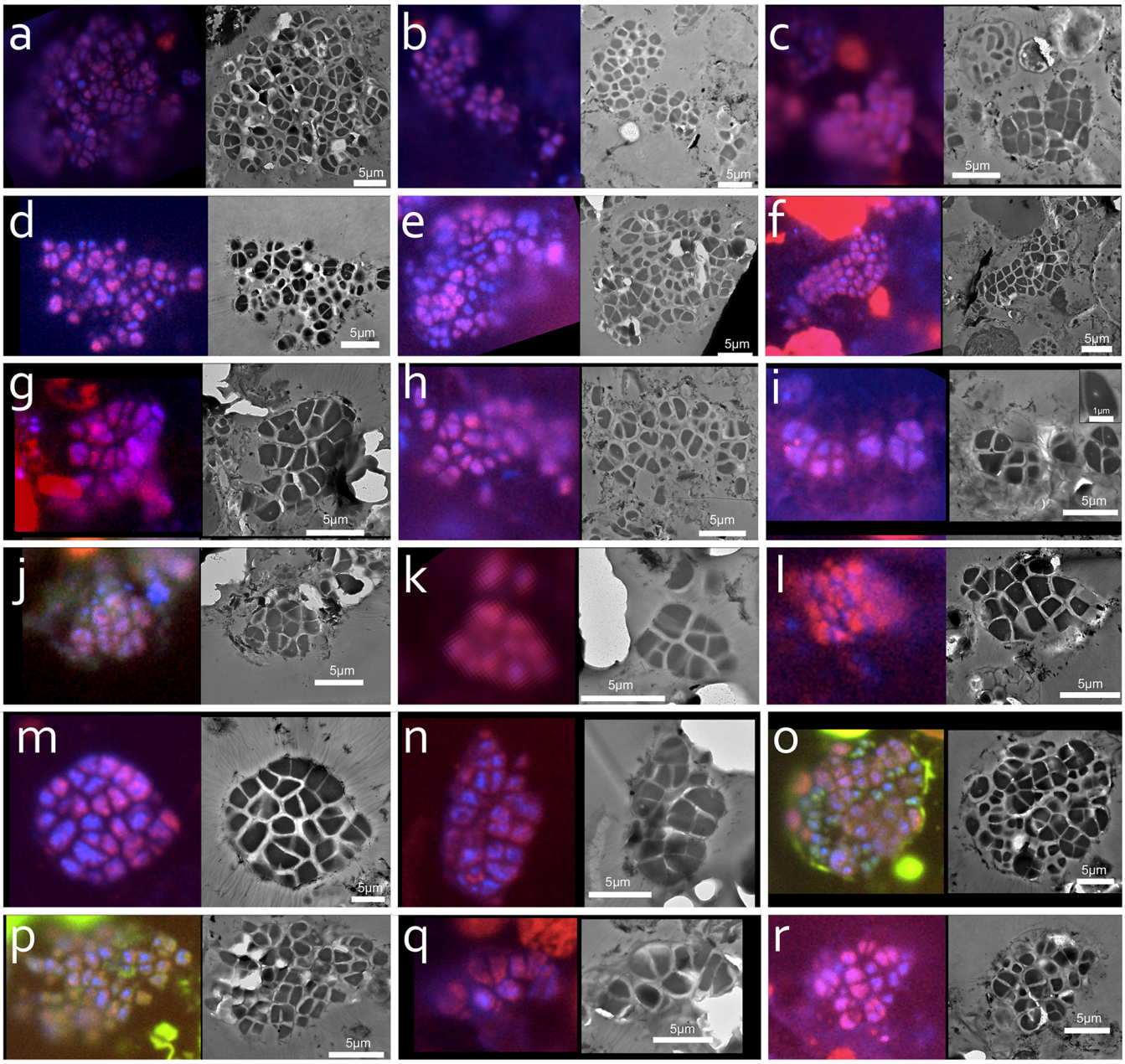

FIG 1 FISH-EM analysis of ANME-2b archaea and deltaproteobacterial consortia recovered from two methane seep sediment incubations. Aggregates were hybridized using a Cy3-labeled ANME-2b-729 probe (shown in red) and a Cy5-labeled DELTA495a probe (shown in green in panels p and o). Aggregates were stained with DAPI (shown in blue). (a to l) Images are from the 5133 methane seep incubation, with aggregate thin sections being approximately 130 nm thick. (m to r) Images are from the 3730 methane seep sample, with aggregate sections of ~170 nm. Scale bars are 5 μm in each panel except for the inset (in which the scale bar is 1 μm).

The finding of pPLG in ANME-2b hybridized cells (observed in all but two FISH-hybridized ANME-2b consortia in Fig. 1), but notably not in other ANME-2 archaeal subgroups hybridized by either the ANME-2-538 or the ANME-2c-760 probes (see below), may be indicative of important ecophysiological differences between the various ANME-2 subgroups. Very little is understood as to how the ANME groups differ from one another or which factors enable coexistence in the same habitat, but if we take a lesson from what is known about the methanogens where different lineages utilize differing enzyme complexes associated with niche adaptation (44, 45), significant diversity in ANME physiology is also likely (46). The function of pPLG found in ANME-2b

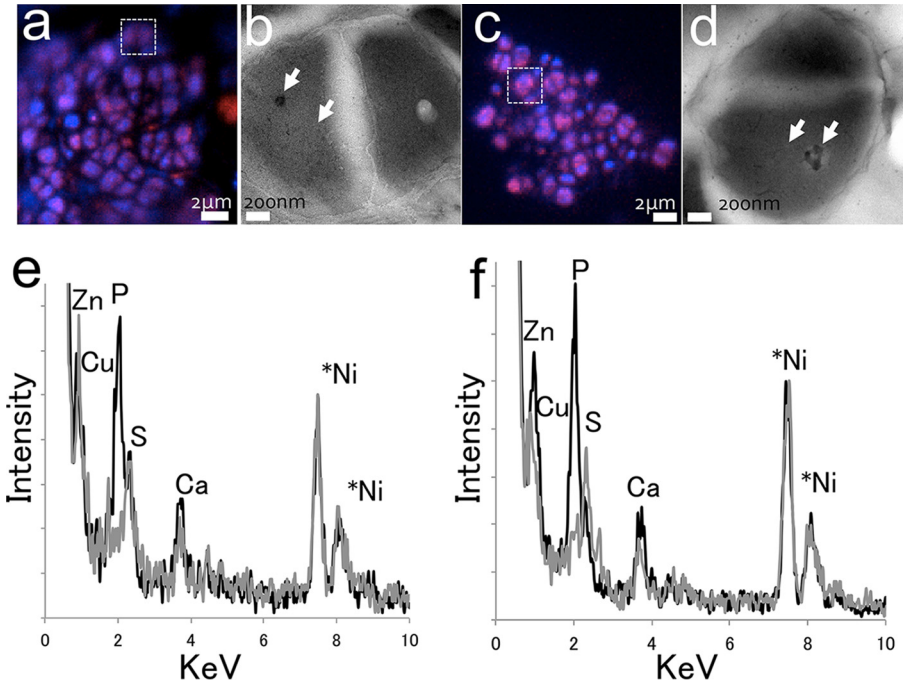

FIG 2 Energy dispersive spectroscopy of ANME-2b cells (red) and associated intracellular polyphosphate-like granules (pPLG) from consortia recovered from sample 5133 (Fig. 1a and d). (a to d) Positively hybridized cells with the ANME-2b-729 probe (a and c) and the corresponding TEM images (b and d). The white boxes in panels a and c indicate where the TEM images were acquired. (e and f) EDS spectra of the granules (black traces) and the cytosol (gray traces) from the areas marked by the white arrows in panels b and d. Six individual ANME-2b cells were analyzed and produced similar spectra. *, note that the Ni in the spectra is derived from the Ni grid on which the thin section was located.

is a target for future investigations, where pPLG content could be monitored as a function of various nutrient regimens, for example.

FISH-EM description of the ultrastructure of non-ANME-2b lineages of ANME-2. The ultrastructures of other ANME-2 consortia (ANME-2a or ANME-2c) recovered from the same sediment sample as the ANME-2b aggregates were also analyzed. These consortia were identified using either a general ANME-2 (ANME-2-538) or clade-specific (ANME-2c-760) oligonucleotide probe. Notably, none of the ANME-2 consortia, aside from those stained by the ANME-2b FISH probe, contained visible pPLG (FISH-TEM observation of more than 20 consortia recovered from two different methane seep sites within Hydrate Ridge). Figure 4 shows ANME-2c-760 and DSS658 probe (*Desulfosarcina/Desulfococcus* [DSS])-hybridized aggregates, and Fig. 5 shows non-ANME-2b aggregates hybridized with the ANME-2-538 and seep1a-1441 probes. Intracellular pPLG were not observed in either of these different ANME-2 aggregate types.

Aggregates shown in Fig. 4a to d were from a FISH hybridization containing 0.01% SDS while 0.01% Triton X-100 was used for panels e and f, but significant differences between these two detergents were not observed. In Fig. 5, only two of the thin-sectioned ANME-2-538 FISH hybridized consortia were observed to associate with the common syntrophic bacterial partner, SEEP-SRB1a (29), targeted with a specific seep1a-1441 FISH probe (Fig. 5b and e). This observation contrasts with earlier findings reported previously in a survey of bacterial partners of ANME from multiple seep sites (29) and with data collected from these same samples in an independent FISH survey of whole aggregates. Using conventional whole-cell FISH, approximately one-half of the ANME-2-538 consortia were found to pair with seep1a-DSS in sample number 5133 (25). Some consortia showed a weak seep1a-DSS Cy5 signal, but high background from adjacent minerals precluded positive identification, or, alternatively, the hybridization signal from this particular probe was not present at sufficient strength in these thin-section samples (~150 nm thick).

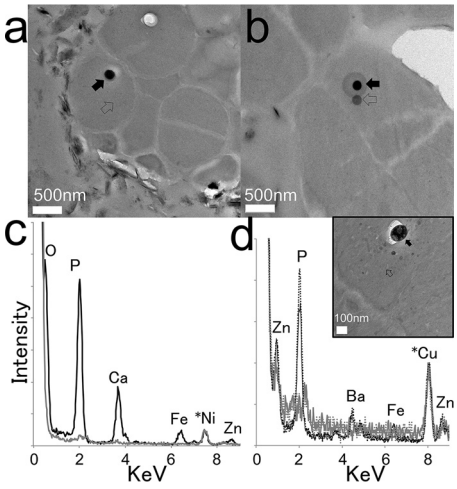

FIG 3 EDS analysis of polyphosphate-like granules (pPLG) in putative ANME-2b aggregates without FISH hybridization. Here, samples were fixed with glutaraldehyde to enhance cellular preservation and granule contents. (a) TEM image of an ~200-nm thin section of an ANME-2 aggregate on an Ni grid from sample 5133. (b and d, inset) TEM images of a second ANME-2 aggregate from the same sample sectioned to ~100 nm thick and transferred onto a Cu grid. (c and d) EDS spectra of the pPLG (black) and cytosol of the cell (gray trace). Shown are two spectra in panel c and four spectra in panel d. In panel d, the trace for the cell shown in the inset in panel d is dashed, and that for the cell depicted in panel b is shown by solid lines. *, Ni and Cu signals in the spectra are derived from the TEM grids the samples are on. Panel b shows a TEM image after EDS acquisition, which caused a blackening of the analyzed area.

Analysis of intracellular magnetosome-like minerals within select ANME-2-associated bacterial partners. In a subset of consortia, bacterial partners in association with ANME-2 archaea hybridized with the general ANME-2-538 probe were observed to contain intracellular magnetosome-like structures (Fig. 5l and u and insets). These magnetosome-containing bacteria did not hybridize positively with the seep1a-specific probe Cy5 signal used here and await phylogenetic identification. They were relatively rare, representing only ~10% of the archaeal-bacterial aggregates screened (2 in 20 consortia) (Fig. 5). Cells were observed in different consortia with one or two magnetosome-like chains (Fig. 5l and u). In the case of two chains, they were visually and compositionally distinct (for example, Fig. 5u, inset). This difference was subsequently shown to be attributable to two distinct material phases identified by energy dispersive spectroscopy (EDS) analysis (Fig. 6). The darker chains were comprised primarily of Fe and S, while the lighter chains were found to be primarily Fe. Presumably this Fe would be coordinated by O; however, the oxygen peak (Kα of 0.525 keV) was occluded in those spectra by a sharp rise at low keV.

Work by Reitner and coworkers (47, 48) also reported the presence of iron sulfide magnetosome-like structures (putatively identified as greigite) by EDS analysis in some of the *Deltaproteobacteria* within the ANME-1-dominated large methanotrophic reef structures discovered in the euxinic Black Sea (49). In that case, only an FeS material was reported, but the coexistence of FeS and FeO in a single cell has been observed before (50, 51), and in the case where mineralogy could be assigned, the presence of greigite and/or magnetite was related to the external environmental conditions and redox potential (52).

The occurrence of magnetosome structures poses questions as to their physiological relevance within ANME-associated bacteria. Generally, magnetosomes in bacteria are thought to function for motility purposes where the alignment of the mineral chain allows cellular orientation with magnetic field lines for taxis and cell positioning within an oxygen gradient (53). Magnetotactic multicellular bacteria are also known to navigate *en masse* (6, 54); however, the magnetosomes in cold seep sediments, such as those observed here, as well as those from the Black Sea (48, 55–57), were not observed to be aligned, implying both that the bacteria cannot move inside consortia and that

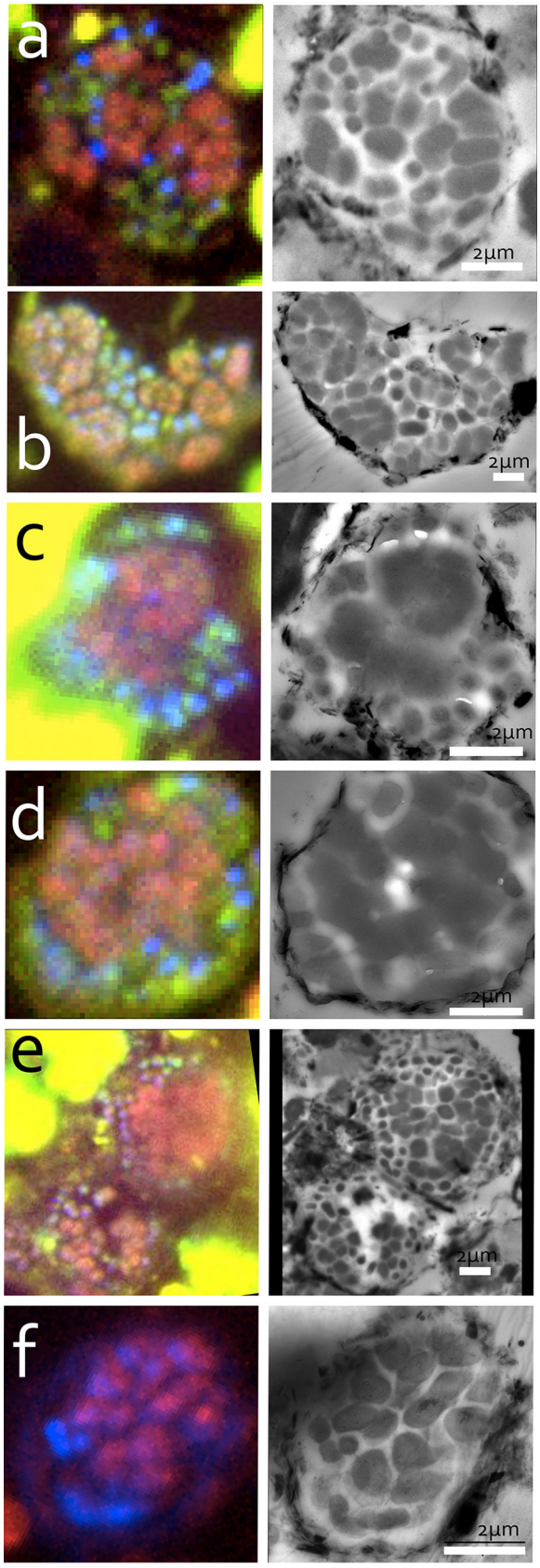

FIG 4 FISH-EM analysis of ANME-2c/bacterial consortia from Hydrate Ridge 5546-5549/5556-5560 samples. ANME-2c aggregates were hybridized with the group-specific ANME-2c_760 probe (red), and

(Continued on next page)

the consortium does not move as a whole, since they should naturally align with the geomagnetic field (58, 59).

An alternative hypothesis for the function of these magnetosome-like structures other than magnetotaxis is based on the idea proposed by Kopp and Kirschvink (60). In that work, the authors noted that intracellular Fe bodies could function as a redox battery, with the cell utilizing this material as an electron donor or acceptor depending on its current physiology. Empirical support for this idea can be seen in *Shewanella putrefaciens* CN32, which stores mixed-valent iron granules (not magnetosomes) which seem to be linked to respiratory activity (61) and may function as an iron lung (62). Such a function seems to fit the observations reported here, where bacteria in association with ANME cells find themselves in the midst of strong redox gradients and may be limited by the diffusion of electron acceptors; as such, the ability to periodically store or draw electrons from an internal source could be a survival strategy based on redox activity rather than a taxis response associated with the Earth's geomagnetic field.

3D serial block face analysis of biovolume and ultrastructure of 2 morphologically distinct ANME-SRB consortia. Conventional TEM and the FISH-EM analysis described here are based on a single cross-section of material in thin section, which lacks valuable information about the morphology, ultrastructure, and biovolume of these complex multicellular consortia in three dimensions (3D). To overcome this limitation, we developed a protocol compatible with high-resolution 3D analysis of environmental consortia recovered directly from sediments using mechanical serial block face scanning electron microscopy (63). This technique allows image acquisition on stacks of planes obtained from the same sample at different depths and, subsequently, 3D reconstruction. Using this technique, cellular biovolumes of ANME and their bacterial partners were measured. In addition, the relationship between pPLG size and cell size was investigated.

Cellular biovolumes of ANME and SRB cell type. The uncultured sediment-hosted ANME bacterial aggregates prepared for serial block face imaging were not identified by FISH, as the introduction of osmium and other contrasting agents used to make samples more conducive to partially reduce sample charging during the analysis rendered the resin opaque and has been shown to damage fluorophores (M. H. Ellisman and T. J. Deerinck, personal communication; see also reference 64 for a recent advance which eliminates charging). In this work, we selected two aggregates, referred to here as consortium number 1 and number 2, representing common morphologies observed in our study (Fig. 7a). Consortium number 1 was analyzed by using 155 images taken at 70-nm steps and had a maximum diameter of 33 μm. Consortium 2 was analyzed by using 188 images taken at 70-nm steps and had a maximum diameter of 22 μm. Archaeal cells in consortium 1 contained pPLG and were tentatively assigned to the ANME-2b subgroup based on our parallel FISH-EM analysis indicating the presence of pPLG in this cell type. The segmented volume of consortium 1 was 530 μm^3 and included 124 archaeal cells and 30 bacterial cells. Consortium 2 was distinguished from consortium 1 by the absence of pPLGs and was broadly classified as associated with the ANME-2 archaea from previous 16S rRNA and FISH analysis of the archaeal diversity within this sample. The segmented volume of consortium 2 contained 55 μm^3 and 30 archaeal and bacterial cells (each). ANME cells in consortium 1 were observed to be, on average, nearly four times larger than the other ANME group in consortium 2 (mean ANME type with pPLG volume, 4.0 μm^3; mean ANME volume without pPLG, 1.1 μm^3). These cells were also larger than either of the bacterial types measured in consortium 1 (mean pPLG ANME paired SRB volume, 0.97 μm^3) or consortium 2 (mean SRB paired with non-pPLG ANME volume, 0.76 μm^3) (Fig. 7b).

FIG 4 Legend (Continued)
coassociated deltaproteobacteria belonging to the *Desulfobacterales* were hybridized using the DSS 658 probe (green). Aggregates were stained using DAPI (blue). The section used in this FISH-EM analysis was ~0.5 μm thick. On the right are corresponding TEM images (scale bars, 2 μm).

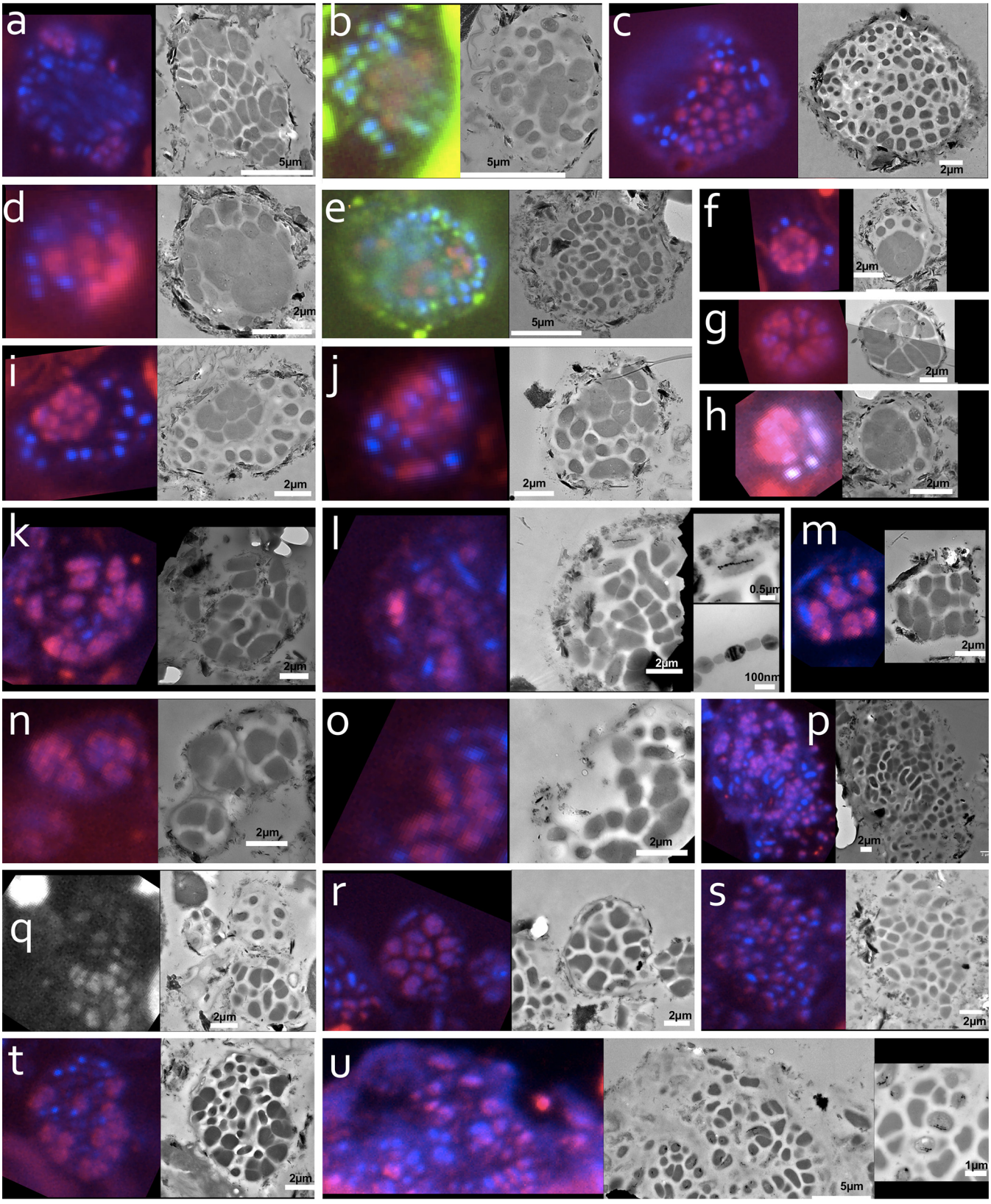

FIG 5 ANME-2 (red) and seep1a or other unidentified bacterial partners (green or blue, respectively). DAPI staining is shown in blue. (a to h) Images are derived from seep samples 5546-5549/5556-5560. The section was blue (~220 nm). (k to u) Images are from seep sample 5133. The section was purple/gold (~150 nm thick). The cells were hybridized with a dual Cy3-labeled ANME-2-538 (27) probe and a dual Cy5-labeled seep1a-1441 probe targeting the most common deltaproteobacterial partner of the ANME-2 (29). Panels l and u contain higher magnification images showing the presence of magnetosomes in these particular ANME-2 partners. Panel q shows the raw FISH image in grayscale in the absence of the DAPI channel. FISH was performed in the presence of 0.005% Triton X-100.

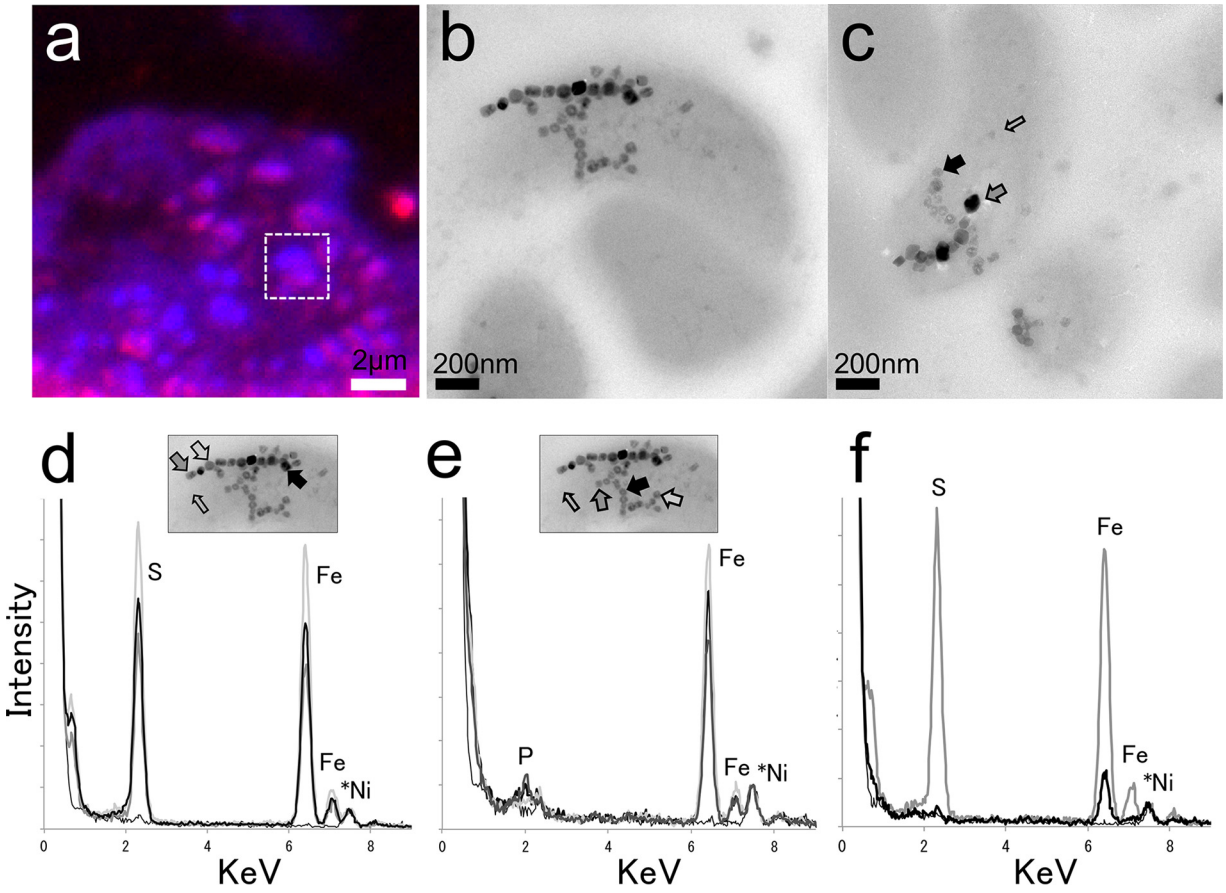

FIG 6 EDS of intracellular mineral phases of bacteria paired with ANME identified by the ANME-2-538 probe. The cells were from the 5133 methane seep sample. (a) FISH image with ANME-2-538 hybridized cells in red and bacterial partners in blue (DAPI). (b) TEM of the boxed region of panel a, where bacteria are positioned at the top of an ANME-2 archaea. (c) Different cells of the same aggregate showing another example of mineral phases in the bacterial cell. (d and e) EDS spectra taken from multiple particles in each of the two chains present in the cell shown in panel b, showing Fe:S composition of the darker material phase in panel b and the absence of S in the lighter phase. Arrows in the image inset above the spectra indicate where the spectra were acquired; arrows and spectra are correlated by shades of gray. (f) Single EDS measurements of each of the chains shown in panel c revealing a similar pattern found in panels d and e, one FeS chain and another without S. Arrows on the TEM images mark the location of EDS acquisition. Panels d, e, and f also contain spectra that were acquired in the cytosol, and no major signal was observed for Fe or S. *, Ni in the spectra is derived from the TEM grid the samples are on.

The volumes of both ANME and SRB measured here with three-dimensional electron microscopy are larger than those in previous reports based on light microscopy (e.g., see references 8 and 65), where volumes were calculated from diameters assuming a spherical shape to be ~0.07 μm^3 for ANME and ~0.03 μm^3 for the SRB. The differences observed here between ANME groups and previous reports may hold implications for modeling and metabolic rate estimation studies (e.g., see references 66 and 67). Furthermore, these differences argue against the application of a universal conversion factor between cell number and biomass (e.g., see references 68 and 69) and indicate the need for coupling individual cell measurements with the appropriate conversion factors (e.g., see reference 70) when estimating the magnitude of these cell's ecological contributions. Finally, the larger variance in size reported here for ANME-2b-like cells compared to the other ANME group is another indication of intragroup variations between ANME.

ANME-2 biovolume of intracellular polyphosphate-like granules is correlated with cell biovolume. Serial block face imaging of consortium 1 revealed that less than 3% of the putative ANME-2b cells lacked intracellular pPLG (4 out of 124 ANME cells). Of the remaining 120 ANME cells, the majority contained one large pPLG, with a subset of ANME containing multiple granules (up to 4 in a cell). Cells with more granules were larger (Fig. 7c), and the volumes of the pPLG were largest in ANME-2 cells containing

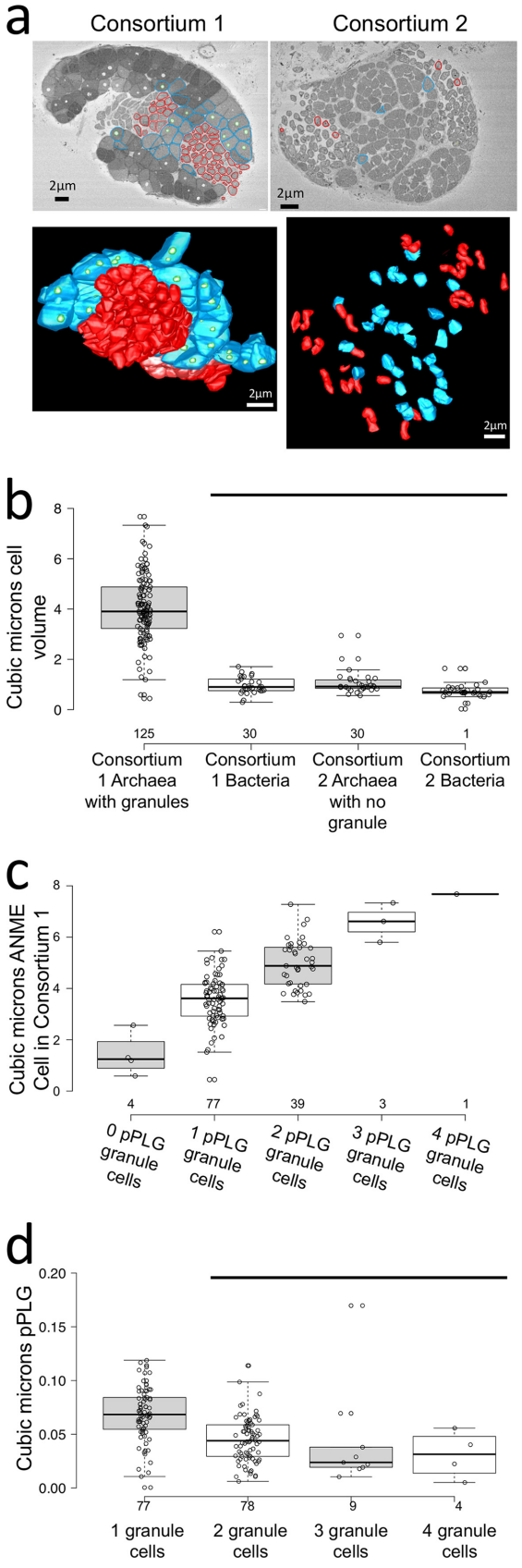

FIG 7 Comparison of cell and polyphosphate-like granule (pPLG) volumes for 2 morphologically distinct ANME-2/bacteria consortia. (a) SEM images acquired during serial block facing of two consortia analyzed

(Continued on next page)

one granule (mean value, 0.069 μm^3 [Fig. 7d]). The individual pPLG volumes in cells containing 2, 3, and 4 granules were similar (mean value, 0.044 μm^3; *P* value of >0.05 by Tukey's honestly significant difference [HSD] test between groups) (Fig. 7d). Interestingly, even though cell size varied significantly within the group of pPLG cells, the average summed volume of these granules was ~1.9% of the total cell volume (Fig. S2). Relationships between cellular polyphosphate and the cell cycle have been observed in bacteria (e.g., see references 71–73), and it will be interesting to examine potential relationships between cell biovolume, pPLG number, and cell cycle in these methanotrophic archaea in future work.

Concluding remarks. Previous efforts to correlate phylogenetic identity to EM observation of microbes were reported as early as 2005, when Gérard and coworkers used whole-cell FISH followed by immunogold detection in mixed pure cultures (74). Later, Halary and coworkers (75) applied 16S rRNA targeted FISH on thin-sectioned, symbiont-bearing metazoans that had been embedded in LR white resin. This work provided a significant advance over the work carried out by Gérard et al. because permeabilization agents were not used, enhancing the preservation of cell ultrastructure. A similar protocol was also used recently on symbiotic poribacteria (76) in combination with freeze substitution and imaging by SEM after epifluorescence and staining with uranyl acetate and lead citrate. Finally, Knierim and coworkers (77) reported the application of catalyzed activity reporter deposition FISH (CARD-FISH) to thin-sectioned material in a manner similar to what Halary and others reported, that is, they performed plastic resin embedding and later applied FISH probes for phylogenetic identification. In addition, that work demonstrated an additional significant advance by applying the CARD-FISH technique to cells on the same TEM grid on which they had previously been imaged by cryoelectron microscopy. In this study, we performed FISH first and followed this by sectioning and imaging by epifluorescence, since FISH after sample embedding was unsuccessful in our hands.

In archaeal AOM systems, the application of epifluorescence microscopy was invaluable for developing models of cellular interactions within this system (for example, see references 11 and 12). Subsequent immunological and histological investigations of the ANME-associated reef structures in the Black Sea with TEM (55, 57) and with epifluorescence microscopy on other Black Sea-derived samples (78) made it possible to verify predictions of which cell types contain which enzymes. TEM observations have also been employed on archaeal AOM systems to gain insight into cell-cell interactions in the form of direct interspecies electron transfer (25, 26).

The morphological and chemical characterization of ANME archaeal groups reported here points to the possibility that substantial physiological differences exist among ANME and their bacterial partners. As shown here, ANME-2b from multiple cores were observed with intracellular polyphosphate like granules, yet ANME-2a/2c cells did not contain these granules. Storage granules also were not reported for "*Candidatus* Methanoperedens nitroreducens" (81). Given the energy-limited nature of this syntrophy and the energetic cost of forming phospho-anhydride linkages, these granules stand out as targets to be investigated in the future. Previous estimations of

FIG 7 Legend (Continued)
in this study. Consortium 1, on the left, is an example of the ANME-2/bacterial aggregate type (putative ANME-2b) with pPLG. Consortium 2, on the right, is an example of an ANME-2/bacterial aggregate lacking intracellular inclusion bodies (likely ANME-2a/2c). Note that the pPLGs on the left appear to be empty, with granule contents likely lost during 3View sample preparation. (b) Comparison of cell volumes of segmented ANME cells (a, blue) and bacterial cells (a, red) from the serial block face image stacks. Each data point represents one cell. (c) Comparison of cell volumes of archaea in consortium 1 to the number of pPLGs contained in the cell. Each data point represents one cell. (d) Individual pPLG volumes compared to the total number of granules observed in the cell. In panels b, c, and d, center lines show the medians; box limits indicate the 25th and 75th percentiles, as determined by R software; whiskers extend 1.5 times the interquartile range from the 25th and 75th percentiles; data points are plotted as open circles. A black bar above the groups in panels b and d links data that are not significantly different ($P > 0.05$ by Tukey's HSD test). The number above or below the *x* axis indicates the number of observations for each category.

ANME-2b and ANME-2c/2a cell doubling times using $^{15}NH_4^+$ stable isotope probing and nanoSIMS revealed that the archaea paired with seep1a bacteria (including ANME-2c/2a) had a mean ^{15}N enrichment value (fractional abundance) of 0.0698, whereas the other archaeal group (including ANME-2b) had a lower mean enrichment value of 0.0525 (*P* value of <0.001 by two-sample *t* test) (25). Whether the observed difference in growth could be related to the energetic cost of phospho-anhydride bond formation for pPLG synthesis or is related to the larger biovolume of the ANME-2b cells remains to be determined.

Another possible differentiating feature between ANME groups has to do with sulfur. From Raman microscopy spectra, it was previously suggested that some ANME-2 archaea contain an intracellular sulfur (S^0) storage capacity, and that partner bacteria contain iron phosphate particles (24). In bacteria, S^0 is stored in intracellular sulfur globules (79), and granules have also been observed in archaea in the *Thermococcales* in association with the membrane and cell surface layer (80). During EDS-based chemical analyses of the ANME-SRB consortia observed in this study, the occurrence of concentrated S in the form of S granules was not detected in ANME archaea, and iron phosphate particles were not detected in partner bacteria. Whether these differences represent examples of physiological or species-specific differences between the diverse environmental ANME and bacterial lineages or is attributed to differences in sample preparation and analytical methodology requires further study.

Very recently, relatives of "*Ca*. Methanoperedens nitroreducens" (16) were studied by electron microscopy (81), and cell diameters of ~1.5 μm were observed using TEM for cells of irregular coccoid morphology. Assuming a spherical shape, this would equate to ~1.7 μm^3, which is in the range of volumes observed here but diverges from the previous estimates based on epifluorescence microscopy (8, 65). Epifluorescence observation of the ANME-SRB consortia analyzed as part of this study yields biovolume estimates that agree with those obtained by TEM (data not shown), arguing against a methodological basis to account for the differences. In addition, recent observations by TEM showed archaea (putative ANME-2c) of the size range observed here paired with bacteria (putative SEEP-SRB2) smaller than those observed here (21). We have yet to fully understand the cause of the apparent size differences between these cells, but physiological and phylogenetic variation could contribute to these observational differences.

Future correlated electron microscopy studies in environmental microbiology will be enhanced if studies integrate (i) EM observables with (ii) molecular phylogeny of individual cells (e.g., FISH), (iii) information on metabolic activity (e.g., with stable isotope probe experiments analyzed by SIMS or Raman), and (iv) functional molecular biology approaches (e.g., by antibody application or mRNA-FISH). By combining these techniques we can better explore microbial activities in the same natural environments that host microbial evolution and are the foundation of microbial biogeochemical cycles. The work reported here on uncultivated subgroups of methane seep sediment-hosted ANME consortia is a step in this direction.

MATERIALS AND METHODS

Site location and sample description. Sediment incubation samples 5133 and 5546-5549/5556-5560 were collected during the R/V *Atlantis* expedition AT 18-10 in August and September of 2011 using the ROV *Jason II* as previously described (25). Sediment incubation 3730 was collected in 2010 during A/V *Atlantis* cruise AT15-68 on dive AD4635 using the HOV *Alvin* as described elsewhere (30, 34).

Chemical fixation of microbial consortia. Fixation protocols were varied for different visualization goals. For the goal of FISH imaging, glutaraldehyde was used at low concentrations. In cases where fluorescence imaging was not a goal, higher glutaraldehyde concentrations were used. Following the fixation procedures described below, samples were subjected to Percoll density separation as described in reference 25, with the exception that HEPES buffer was substituted for phosphate-buffered saline (PBS).

Sample preparation for FISH-EM. The primary fixative mixture was prepared by mixing 5 ml 20% paraformaldehyde from a sealed glass ampule (EMS; EM grade and methanol free) and 0.25 ml 10% glutaraldehyde (EMS; EM grade and methanol free) with 7.25 ml of 0.22-μm filtered 50 mM HEPES, pH 7.4, 35 g/liter NaCl in NANOpure water to achieve a final volume of 12.5 ml. The final concentrations were 8% paraformaldehyde, 0.2% glutaraldehyde, 29 mM HEPES, and 20 g/liter NaCl. The low concentration

of glutaraldehyde was chosen to prevent glutaraldehyde-derived autofluorescence. This fixative solution was then aliquoted into 1-ml volumes and frozen in 1.7-ml Eppendorf tubes at −80°C until further use. For fixation of consortia in sediment, an aliquot of the sediment slurry was removed with a sterile disposable needle and syringe from the overpressurized microcosm incubations and immediately mixed 1:1 volumetrically with the aldehyde fixative on ice in 2-ml Eppendorf tubes (final concentrations in the tube of 4% paraformaldehyde, 0.1% glutaraldehyde, 14.5 mM HEPES, pH 7.4, 10 g/liter NaCl). The tubes were incubated for 60 min on ice and periodically inverted to mix during the fixation period.

After fixation, the slurry was centrifuged at 2,000 × *g* in an Eppendorf microcentrifuge for 1 min, and the supernatant was removed and replaced with ~1.8 ml 50 mM HEPES, pH 7.4, 35 g/liter NaCl (enough buffer to fill the 2-ml centrifuge tube). This was repeated for a total of four buffer replacements to remove traces of fixative, and after the final replacement, the sediment was resuspended in 500 μl of 50 mM HEPES, pH 7.4, 35 g/liter NaCl and stored at 4°C until further use. We recommend using the fixed material immediately for FISH (as was done for the images shown in Fig. 1). However, we found that hybridization of the ANME-*Deltaproteobacteria* consortia was stable for at least 10 days in buffer (as was done for Fig. 2 and 3; longer periods of time were not tested).

Fixation of samples for traditional TEM and energy-dispersive X-ray spectral analyses. Sediment was fixed by adding one volume of 5% glutaraldehyde (EMS) in 25 mM HEPES buffer (pH 7.5) containing 17.5 g/liter NaCl to the sediment. The sample was left on ice for 1 to 3.5 h during fixation and then processed as described above for FISH (aldehyde was removed by sequential buffer resuspensions and centrifugations).

Fixation of samples for SBEM. Sediment slurry was directly fixed on ice for 1 h, using final concentrations in the tube of 2.5% glutaraldehyde and 2% paraformaldehyde, 7.25 mM HEPES, pH 7.5, 5 g/liter NaCl, and then processed as described above for FISH (aldehyde was removed by sequential buffer resuspensions and centrifugations).

FISH hybridization of consortia bound in noble agar. FISH hybridization was carried out on microbial consortia which were bound in blocks of noble agar as prepared in reference 25. This procedure was adopted to achieve high concentrations of aggregates which could be visualized later and to facilitate transfer of buffers between hybridization steps. Between 2 and 3 agar blocks containing concentrated aggregates from the Percoll density separation described above were submerged in a single 1.7-ml Eppendorf tube containing 200 μl of FISH hybridization buffer. FISH hybridization stringency was adjusted in the hybridization and wash buffers by varying the concentrations of formamide and NaCl solutions depending on the oligonucleotide probes used (Table 1) (82, 83). High-performance liquid chromatography (HPLC)-purified oligonucleotide probes were purchased from Integrated DNA Technologies (IDT) with fluorophores attached to the 5′ and 3′ ends (DOPE-FISH) (84). The final fluorescent oligonucleotide probe concentration in the hybridization solutions was 2.5 ng/μl. Triton X-100 is a commonly used detergent for electron microscopy preparations (85), and in the experiments described here, 0.005% Triton X-100 was used in the hybridization buffer in place of the 0.01% SDS that is typically used during FISH. Hybridization was conducted at 46°C for 60 to 90 min in a hybridization oven, after which the hybridization buffer was removed and replaced with 1 ml wash buffer adjusted to match the formamide concentration (82, 83) in a 48°C water bath. This wash buffer was replaced three times over a period of 15 min. The first two additions and removals of wash buffer were performed as quickly as possible, with the tubes maintained in Styrofoam holders to minimize temperature fluctuations. After the third addition, the samples were placed back into the water bath for the remainder of the 15-min period (~8 min). After this period, the wash buffer was removed and the agar blocks were transferred into 1 ml of 50 mM HEPES, pH 7.4, 35 g/liter NaCl, followed by immediate embedding in LR white resin as described below.

LR white embedding of microbial consortia for FISH-EM and traditional TEM. A protocol for embedding consortia in LR white resin for thin sectioning was adapted from reference 86. Agar blocks containing FISH hybridized microbial consortia were dehydrated in 1.7-ml Eppendorf tubes through a graded ethanol series (25%, 50%, 75%, and 100%) with three 100% ethanol solution changes. Solutions were changed with 1-ml additions and occurred for 15 min with slow mixing on a rocker table for each step. The ethanol solutions were made by diluting 100% ethanol into 50 mM HEPES (pH 7.6). Following the dehydration series, samples were transferred into 50% LR white resin, 50% ethanol and incubated at room temperature on a rocker for 30 min. This solution was then exchanged for 100% LR white resin and incubated again for 1 h on a rocker. At the end of the incubation, the LR white resin was exchanged with 1 ml of fresh LR white resin (100%), the Eppendorf tubes were capped, and the agar blocks with consortia were placed in a 58°C oven for 2 days. Before polymerization, an attempt was made to orient the agar block face containing consortia face down at the bottom of the tube, although this is not strictly necessary. After 2 days, if the sample had not hardened appropriately, it was placed back in the oven overnight, after which time polymerization was achieved.

Staining and embedding of cells for SBEM. The staining and embedding protocol was adapted from the original one developed at the National Center for Microscopy and Imaging Research (NCMIR; UC San Diego, San Diego, CA) for serial block face scanning electron microscopy of biological tissue specimens (87, 88). After fixation, Percoll separation, and immobilization in noble agar (described above and in reference 25), microbial consortia were subjected to a heavy-metal staining protocol to achieve conductivity and contrast (87). Right before use, a solution containing 3% potassium ferrocyanide in 0.3 M cacodylate buffer with 4 mM calcium chloride was combined with an equal volume of 4% aqueous osmium tetroxide (EMS). The agar blocks sat in this solution for 1 h on ice.

Thiocarbohydrazide (TCH) solution was then freshly prepared by adding 0.1 g thiocarbohydrazide (Ted Pella) to 10 ml double-distilled water (ddH_2O) in a 60°C oven for 1 h and agitating periodically. The

solution was filtered through a 0.22-μm Millipore syringe filter. At the end of the osmium tetroxide incubation, the samples were washed with ddH_2O at room temperature 5 times for 3 min each time (~15 min total) and then incubated in the filtered TCH solution for 20 min at room temperature. The samples were then rinsed again 5 times for 3 min each in ddH_2O at room temperature and thereafter placed in 2% osmium tetroxide (not osmium ferrocyanide) in ddH_2O for 30 min at room temperature. Following this second exposure to osmium, the cells were washed 5 times for 3 min each time at room temperature in ddH_2O and then placed in 1% uranyl acetate (aqueous) and left in a refrigerator (~4°C) overnight. The next day, *en bloc* staining with Walton's lead aspartate staining was performed by dissolving 0.998 g of L-aspartic acid (Sigma-Aldrich) in 250 ml of ddH_2O. Lead nitrate (0.066 g) was then added to 10 ml of aspartic acid solution, and the pH was adjusted to 5.5 with 1N KOH. The lead aspartate solution was placed in a 60°C oven for 30 min. The cells were washed 5 times for 3 min each time in ddH_2O at room temperature, placed in the lead aspartate solution, and then returned to the oven for 30 min. The cells were then washed 5 times for 3 min each in room temperature ddH_2O and dehydrated using ice-cold solutions of freshly prepared 20%, 50%, 70%, 90%, and 100% (two separate additions of 100%) anhydrous ethanol for 5 min each, placed in anhydrous ice-cold acetone, and left at room temperature for 10 min.

Durcupan ACM resin (EMS) was formulated by weight as 11.4 g part A, 10 g part B, 0.3 g part C, and 0.05 to 0.1 g part D, yielding a hard resin when polymerized. The resin was mixed thoroughly. Samples were placed into 25% Durcupan-acetone for 2 h, into 50% Durcupan-acetone for 2 h, and then into 75% Durcupan-acetone for 2 h. The cells were placed in 100% Durcupan overnight and then into fresh 100% Durcupan for 2 h. The agar blocks were then embedded in a thin layer of fresh resin in an aluminum weigh boat and placed in a 60°C oven for 48 h.

Sectioning of resin-embedded consortia. Resin blocks containing concentrated microbial consortia were cut into thin sections, ranging from 100 nm to 500 nm, using a Leica Ultracut UCT ultramicrotome equipped with a diamond knife. The sectioning was done with the knife positioned parallel to the layer of concentrated microbial consortia, so that the maximum amount of consortia could be observed on each section. Sections were floated on water and placed on Ni or Cu London Finder 135 grids (EMS) which had been briefly exposed to a flame to become hydrophilic. For correlated light-electron microscopy, glow-discharged Formvar/carbon-coated grids were used. For samples designated only for electron microscopy analysis, uncoated grids were used after being briefly flamed with a cigarette lighter and rinsed in deionized water to make them hydrophilic.

Epifluorescence microscopy. Sections on grids were placed in a 46°C oven for at least 1 h after sectioning to ensure LR white sections adhered to the TEM grids through subsequent handling steps. The grids were then mounted on a glass microscope slide containing a drop (3 μl) of 5 μg/ml 4′,6-diamidino-2-phenylindole (DAPI) mixed in Vectashield mounting medium (89). After floating the grid onto the droplet, another (~2 μl) droplet of the DAPI-Vectashield mixture was placed directly on top of the grid and covered with a coverslip. Slides were viewed on an upright epifluorescence Olympus BX51 microscope equipped with the following Olympus objectives: Uplan FLN 100×/1.3 oil ∞/0.17/FN 26.5 UIS2, PlanApoN 60×/1.42 oil ∞/0.17/FN 26.5 UIS2 BFP 1, and UPlanFL N 10×/0.30 Ph1 ∞/-/FN26.5. The light source was an X-Cite 120 Q, and typically images were acquired at an illumination setting of 25% maximum lamp intensity and a camera gain setting of 10. QImaging's Q-capture Pro software was used for image acquisition. The order of image acquisitions was Cy5, Cy3, 6-carboxyfluorescein, and finally DAPI, motivated by the idea that Cy5 dyes often photobleach but DAPI is robust in comparison. A 10× image taken in the DAPI channel was used for orientation during subsequent TEM analyses. The grids were removed from the microscope slide by gently sliding off the coverslip, nudging the grid to the edge of the microscope slide, and gently picking the grid up with tweezers, taking care not to bend the grid. The DAPI solution was removed by briefly dipping the grid into a container of Millipore water. The grid was then dried by wicking the water away with a piece of Whatman filter paper. The analyzed and dried grid was then stored in a TEM grid box at room temperature for subsequent TEM analysis.

TEM analyses. Electron microscopy images of FISH hybridized consortia were acquired using a JEOL JEM-Z3200EF TEM operated at 300 kV. Conventional transmission electron microscopy (4K by 4K; 16 megapixel) and zero-loss energy-filtered transmission electron microscopy (4K by 4K) images were acquired using a Gatan UltraScan 4000 charge-coupled device (CCD) camera. Alternatively, samples for energy-dispersive analysis (EDS) were imaged using an FEI Tecnai Spirit TEM operated at 120 kV. Conventional transmission electron microscopy images (2K by 2K) were acquired using a TVIPS F224 CCD camera. EDS analyses were performed on a Tecnai F30ST operated at 300 kV. The EDS system used was an Oxford INCA.

Analysis of consortia with SBEM. Specimens were cut out of the Durcupan resin blocks, precision trimmed with a glass knife, mounted on aluminum pins, and imaged using a Zeiss Merlin compact scanning electron microscope fitted with a serial block face sectioning system (3View; Gatan, Inc.). Specimens were imaged at 3 keV in a 30-Pa pressure chamber to reduce specimen charging, using 70-nm cutting intervals. Image stacks were converted to 8 bit for analysis and for manual segmentation of individual cells using IMOD software (Boulder Laboratory for 3-D Electron Microscopy of Cells, University of Colorado, Boulder, CO) (90–92). Objects were segmented at various slice intervals, and the resulting data were plotted using BoxPlotR, a web tool for generation of box plots (http://shiny.chemgrid.org/boxplotr/) (93, 94). Statistical analyses were carried out with the online calculator at http://astatsa.com/ and using analysis of variance (ANOVA) with *post hoc* Tukey's HSD and the Tukey-Kramer formula.

SUPPLEMENTAL MATERIAL

Supplemental material for this article may be found at https://doi.org/10.1128/AEM.00399-18.

SUPPLEMENTAL FILE 1, PDF file, 2.0 MB.

ACKNOWLEDGMENTS

We are grateful for the use of the facilities of the Beckman Resource Center for Transmission Electron Microscopy at Caltech (BRCem) and helpful advice from Alasdair McDowall and Mark Ladinsky. This work also benefited from the Applied Physics and Materials Science Department's Transmission Electron Microscopy Facility at Caltech, where EDS measurements were made with Carol M. Garland.

This work was funded by the U.S. Department of Energy, Office of Science, Office of Biological Environmental Research, under award numbers DE-SC0004949 and DE-SC0010574 and by a grant from the Gordon and Betty Moore Foundation Marine Microbiology Initiative (grant number 3780), both to V.J.O. S.E.M. was supported in part by an MEXT KAKENHI Grant-in-Aid for challenging exploratory research (grant award number 15K14608) and the Research Foundation for Opto-Science and Technology. New correlated microscopy and 3D EM method development, as well as access to advanced imaging resources housed at UCSD, was supported by a grant from the NIH National Institute of General Medical Sciences (number P41GM103412 to M.H.E.), an award which partially supports the National Center for Microscopy and Imaging Research.

REFERENCES

1. Hug LA, Baker BJ, Anantharaman K, Brown CT, Probst AJ, Castelle CJ, Butterfield CN, Hernsdorf AW, Amano Y, Ise K, Suzuki Y, Dudek N, Relman DA, Finstad KM, Amundson R, Thomas BC, Banfield JF. 2016. A new view of the tree of life. Nat Microbiol 1:16048. https://doi.org/10.1038/nmicrobiol.2016.48.
2. Parks DH, Rinke C, Chuvochina M, Chaumeil P-A, Woodcroft BJ, Evans PN, Hugenholtz P, Tyson GW. 2017. Recovery of nearly 8,000 metagenome-assembled genomes substantially expands the tree of life. Nat Microbiol 2:1533. https://doi.org/10.1038/s41564-017-0012-7.
3. Moissl C, Rachel R, Briegel A, Engelhardt H, Huber R. 2005. The unique structure of archaeal "hami," highly complex cell appendages with nano-grappling hooks. Mol Microbiol 56:361–370. https://doi.org/10.1111/j.1365-2958.2005.04294.x.
4. Perras AK, Daum B, Ziegler C, Takahashi LK, Ahmed M, Wanner G, Klingl A, Leitinger G, Kolb-Lenz D, Gribaldo S, Auerbach A, Mora M, Probst AJ, Bellack A, Moissl-Eichinger C. 2015. S-layers at second glance? Altiarchaeal grappling hooks (hami) resemble archaeal S-layer proteins in structure and sequence. Front Microbiol 6:543.
5. Comolli LR, Baker BJ, Downing KH, Siegerist CE, Banfield JF. 2009. Three-dimensional analysis of the structure and ecology of a novel, ultra-small archaeon. ISME J 3:159–167. https://doi.org/10.1038/ismej.2008.99.
6. Keim CN, Abreu F, Lins U, de Barros HL, Farina M. 2004. Cell organization and ultrastructure of a magnetotactic multicellular organism. J Struct Biol 145:254–262. https://doi.org/10.1016/j.jsb.2003.10.022.
7. van Niftrik L, Geerts WJC, van Donselaar EG, Humbel BM, Webb RI, Fuerst JA, Verkleij AJ, Jetten MSM, Strous M. 2008. Linking ultrastructure and function in four genera of anaerobic ammonium-oxidizing bacteria: cell plan, glycogen storage, and localization of cytochrome C proteins. J Bacteriol 190:708–717. https://doi.org/10.1128/JB.01449-07.
8. Boetius A, Ravenschlag K, Schubert CJ, Rickert D, Widdel F, Gieseke A, Amann R, Jørgensen BB, Witte U, Pfannkuche O. 2000. A marine microbial consortium apparently mediating anaerobic oxidation of methane. Nature 407:623–626. https://doi.org/10.1038/35036572.
9. Orphan VJ, Hinrichs KU, Ussler W, Paull CK, Taylor LT, Sylva SP, Hayes JM, Delong EF. 2001. Comparative analysis of methane-oxidizing archaea and sulfate-reducing bacteria in anoxic marine sediments. Appl Environ Microbiol 67:1922–1934. https://doi.org/10.1128/AEM.67.4.1922-1934.2001.
10. Nauhaus K, Boetius A, Krüger M, Widdel F. 2002. In vitro demonstration of anaerobic oxidation of methane coupled to sulphate reduction in sediment from a marine gas hydrate area. Environ Microbiol 4:296–305. https://doi.org/10.1046/j.1462-2920.2002.00299.x.
11. Orphan VJ, House CH, Hinrichs K-U, McKeegan KD, DeLong EF. 2002. Multiple archaeal groups mediate methane oxidation in anoxic cold seep sediments. Proc Natl Acad Sci U S A 99:7663–7668. https://doi.org/10.1073/pnas.072210299.
12. Knittel K, Lösekann T, Boetius A, Kort R, Amann R. 2005. Diversity and distribution of methanotrophic archaea at cold seeps. Appl Environ Microbiol 71:467–479. https://doi.org/10.1128/AEM.71.1.467-479.2005.
13. Hallam SJ, Putnam N, Preston CM, Detter JC, Rokhsar D, Richardson PM, DeLong EF. 2004. Reverse methanogenesis: testing the hypothesis with environmental genomics. Science 305:1457–1462. https://doi.org/10.1126/science.1100025.
14. Meyerdierks A, Kube M, Lombardot T, Knittel K, Bauer M, Glöckner FO, Reinhardt R, Amann R. 2005. Insights into the genomes of archaea mediating the anaerobic oxidation of methane. Environ Microbiol 7:1937–1951. https://doi.org/10.1111/j.1462-2920.2005.00844.x.
15. Meyerdierks A, Kube M, Kostadinov I, Teeling H, Glöckner FO, Reinhardt R, Amann R. 2010. Metagenome and mRNA expression analyses of anaerobic methanotrophic archaea of the ANME-1 group. Environ Microbiol 12:422–439. https://doi.org/10.1111/j.1462-2920.2009.02083.x.
16. Haroon MF, Hu S, Shi Y, Imelfort M, Keller J, Hugenholtz P, Yuan Z, Tyson GW. 2013. Anaerobic oxidation of methane coupled to nitrate reduction in a novel archaeal lineage. Nature 500:567–570. https://doi.org/10.1038/nature12375.
17. Wang F-P, Zhang Y, Chen Y, He Y, Qi J, Hinrichs K-U, Zhang X-X, Xiao X, Boon N. 2014. Methanotrophic archaea possessing diverging methane-oxidizing and electron-transporting pathways. ISME J 8:1069–1078. https://doi.org/10.1038/ismej.2013.212.
18. Arshad A, Speth DR, de Graaf RM, Op den Camp HJM, Jetten MSM, Welte CU. 2015. A metagenomics-based metabolic model of nitrate-dependent anaerobic oxidation of methane by methanoperedens-like archaea. Front Microbiol 6:1423. https://doi.org/10.3389/fmicb.2015.01423.
19. Skennerton CT, Chourey K, Iyer R, Hettich RL, Tyson GW, Orphan VJ. 2017. Methane-fueled syntrophy through extracellular electron transfer: uncovering the genomic traits conserved within diverse bacterial partners of anaerobic methanotrophic archaea. mBio 8:e00530-17. https://doi.org/10.1128/mBio.00530-17.
20. Wegener G, Krukenberg V, Ruff SE, Kellermann MY, Knittel K. 2016.

Metabolic capabilities of microorganisms involved in and associated with the anaerobic oxidation of methane. Front Microbiol 7:46. https://doi.org/10.3389/fmicb.2016.00046.
21. Krukenberg V, Harding K, Richter M, Glöckner FO, Gruber-Vodicka HR, Adam B, Berg JS, Knittel K, Tegetmeyer HE, Boetius A, Wegener G. 2016. Candidatus Desulfofervidus auxilii, a hydrogenotrophic sulfate-reducing bacterium involved in the thermophilic anaerobic oxidation of methane. Environ Microbiol 18:3073–3091. https://doi.org/10.1111/1462-2920.13283.
22. Dekas AE, Poretsky RS, Orphan VJ. 2009. Deep-sea archaea fix and share nitrogen in methane-consuming microbial consortia. Science 326:422–426. https://doi.org/10.1126/science.1178223.
23. Orphan VJ, Turk KA, Green AM, House CH. 2009. Patterns of 15N assimilation and growth of methanotrophic ANME-2 archaea and sulfate-reducing bacteria within structured syntrophic consortia revealed by FISH-SIMS. Environ Microbiol 11:1777–1791. https://doi.org/10.1111/j.1462-2920.2009.01903.x.
24. Milucka J, Ferdelman TG, Polerecky L, Franzke D, Wegener G, Schmid M, Lieberwirth I, Wagner M, Widdel F, Kuypers MMM. 2012. Zero-valent sulphur is a key intermediate in marine methane oxidation. Nature 491:541–546.
25. McGlynn SE, Chadwick GL, Kempes CP, Orphan VJ. 2015. Single cell activity reveals direct electron transfer in methanotrophic consortia. Nature 526:531–535. https://doi.org/10.1038/nature15512.
26. Wegener G, Krukenberg V, Riedel D, Tegetmeyer HE, Boetius A. 2015. Intercellular wiring enables electron transfer between methanotrophic archaea and bacteria. Nature 526:587–590. https://doi.org/10.1038/nature15733.
27. Treude T, Knittel K, Blumenberg M, Seifert R, Boetius A. 2005. Subsurface microbial methanotrophic mats in the Black Sea. Appl Environ Microbiol 71:6375–6378. https://doi.org/10.1128/AEM.71.10.6375-6378.2005.
28. Macalady JL, Lyon EH, Koffman B, Albertson LK, Meyer K, Galdenzi S, Mariani S. 2006. Dominant microbial populations in limestone-corroding stream biofilms, Frasassi cave system, Italy. Appl Environ Microbiol 72:5596–5609. https://doi.org/10.1128/AEM.00715-06.
29. Schreiber L, Holler T, Knittel K, Meyerdierks A, Amann R. 2010. Identification of the dominant sulfate-reducing bacterial partner of anaerobic methanotrophs of the ANME-2 clade. Environ Microbiol 12:2327–2340.
30. Hatzenpichler R, Connon SA, Goudeau D, Malmstrom RR, Woyke T, Orphan VJ. 2016. Visualizing in situ translational activity for identifying and sorting slow-growing archaeal-bacterial consortia. Proc Natl Acad Sci U S A 113:E4069–E4078. https://doi.org/10.1073/pnas.1603757113.
31. Manz W, Eisenbrecher M, Neu TR, Szewzyk U. 1998. Abundance and spatial organization of Gram-negative sulfate-reducing bacteria in activated sludge investigated by in situ probing with specific 16S rRNA targeted oligonucleotides. FEMS Microbiol Ecol 25:43–61. https://doi.org/10.1111/j.1574-6941.1998.tb00459.x.
32. Loy A, Lehner A, Lee N, Adamczyk J, Meier H, Ernst J, Schleifer K-H, Wagner M. 2002. Oligonucleotide microarray for 16S rRNA gene-based detection of all recognized lineages of sulfate-reducing prokaryotes in the environment. Appl Environ Microbiol 68:5064–5081. https://doi.org/10.1128/AEM.68.10.5064-5081.2002.
33. Miyashita A, Mochimaru H, Kazama H, Ohashi A, Yamaguchi T, Nunoura T, Horikoshi K, Takai K, Imachi H. 2009. Development of 16S rRNA gene-targeted primers for detection of archaeal anaerobic methanotrophs (ANMEs). FEMS Microbiol Lett 297:31–37. https://doi.org/10.1111/j.1574-6968.2009.01648.x.
34. Trembath-Reichert E, Green-Saxena A, Orphan VJ. 2013. Chapter two–whole cell immunomagnetic enrichment of environmental microbial consortia using rRNA-targeted magneto-FISH, p 21–44. *In* DeLong, EF (ed), Methods in enzymology. Academic Press, Inc, San Diego, CA.
35. Robinson RW. 1986. Life cycles in the methanogenic Archaebacterium Methanosarcina mazei. Appl Environ Microbiol 52:17–27.
36. Seufferheld M, Vieira MCF, Ruiz FA, Rodrigues CO, Moreno SNJ, Docampo R. 2003. Identification of organelles in bacteria similar to acidocalcisomes of unicellular eukaryotes. J Biol Chem 278:29971–29978. https://doi.org/10.1074/jbc.M304548200.
37. Seufferheld M, Lea CR, Vieira M, Oldfield E, Docampo R. 2004. The H+-pyrophosphatase of Rhodospirillum rubrum is predominantly located in polyphosphate-rich acidocalcisomes. J Biol Chem 279:51193–51202. https://doi.org/10.1074/jbc.M406099200.
38. Scherer PA, Bochem HP. 1983. Energy-dispersive X-ray microanalysis of the methanogen Methanosarcina barkeri "Fusaro" grown on methanol and in the presence of heavy metals. Curr Microbiol 9:187–193. https://doi.org/10.1007/BF01567579.
39. Scherer PA, Bochem HP. 1983. Ultrastructural investigation of 12 Methanosarcinae and related species grown on methanol for occurrence of polyphosphatelike inclusions. Can J Microbiol 29:1190–1199. https://doi.org/10.1139/m83-182.
40. Toso DB, Henstra AM, Gunsalus RP, Zhou ZH. 2011. Structural, mass and elemental analyses of storage granules in methanogenic archaeal cells. Environ Microbiol 13:2587–2599. https://doi.org/10.1111/j.1462-2920.2011.02531.x.
41. Rudnick H, Hendrich S, Pilatus U, Blotevogel K-H. 1990. Phosphate accumulation and the occurrence of polyphosphates and cyclic 2,3-diphosphoglycerate in Methanosarcina frisia. Arch Microbiol 154:584–588. https://doi.org/10.1007/BF00248840.
42. Zhang H, Ishige K, Kornberg A. 2002. A polyphosphate kinase (PPK2) widely conserved in bacteria. Proc Natl Acad Sci U S A 99:16678–16683. https://doi.org/10.1073/pnas.262655199.
43. Achbergerová L, Nahálka J. 2014. PPK1 and PPK2–which polyphosphate kinase is older? Biologia (Bratisl) 69:263–269.
44. Thauer RK, Kaster A-K, Seedorf H, Buckel W, Hedderich R. 2008. Methanogenic archaea: ecologically relevant differences in energy conservation. Nat Rev Microbiol 6:579–591. https://doi.org/10.1038/nrmicro1931.
45. Welte C, Deppenmeier U. 2014. Bioenergetics and anaerobic respiratory chains of aceticlastic methanogens. Biochim Biophys Acta 1837:1130–1147. https://doi.org/10.1016/j.bbabio.2013.12.002.
46. McGlynn SE. 2017. Energy metabolism during anaerobic methane oxidation in ANME archaea. Microbes Environ 32:5–13. https://doi.org/10.1264/jsme2.ME16166.
47. Reitner J, Peckmann J, Reimer A, Schumann G, Thiel V. 2005. Methane-derived carbonate build-ups and associated microbial communities at cold seeps on the lower Crimean shelf (Black Sea). Facies 51:66–79. https://doi.org/10.1007/s10347-005-0059-4.
48. Reitner J, Peckmann J, Blumenberg M, Michaelis W, Reimer A, Thiel V. 2005. Concretionary methane-seep carbonates and associated microbial communities in Black Sea sediments. Palaeogeogr Palaeoclimatol Palaeoecol 227:18–30. https://doi.org/10.1016/j.palaeo.2005.04.033.
49. Michaelis W, Seifert R, Nauhaus K, Treude T, Thiel V, Blumenberg M, Knittel K, Gieseke A, Peterknecht K, Pape T, Boetius A, Amann R, Jørgensen BB, Widdel F, Peckmann J, Pimenov NV, Gulin MB. 2002. Microbial reefs in the Black Sea fueled by anaerobic oxidation of methane. Science 297:1013–1015. https://doi.org/10.1126/science.1072502.
50. Bazylizinki DA, Heywood BR, Mann S, Frankel RB. 1993. Fe304 and Fe3S4 in a bacterium. Nature 366:218–218. https://doi.org/10.1038/366218a0.
51. Bazylinski DA, Frankel RB, Heywood BR, Mann S, King JW, Donaghay PL, Hanson AK. 1995. Controlled biomineralization of magnetite (Fe_3O_4) and greigite (Fe_3S_4) in a magnetotactic bacterium. Appl Environ Microbiol 61:3232–3239.
52. Lefèvre CT, Menguy N, Abreu F, Lins U, Pósfai M, Prozorov T, Pignol D, Frankel RB, Bazylinski DA. 2011. A cultured greigite-producing magnetotactic bacterium in a novel group of sulfate-reducing bacteria. Science 334:1720–1723. https://doi.org/10.1126/science.1212596.
53. Faivre D, Schüler D. 2008. Magnetotactic bacteria and magnetosomes. Chem Rev 108:4875–4898. https://doi.org/10.1021/cr078258w.
54. Leao P, Chen Y-R, Abreu F, Wang M, Zhang W-J, Zhou K, Xiao T, Wu L-F, Lins U. 2017. Ultrastructure of ellipsoidal magnetotactic multicellular prokaryotes depicts their complex assemblage and cellular polarity in the context of magnetotaxis. Environ Microbiol 19:2151–2163. https://doi.org/10.1111/1462-2920.13677.
55. Heller C, Hoppert M, Reitner J. 2008. Immunological localization of coenzyme M reductase in anaerobic methane-oxidizing archaea of ANME 1 and ANME 2 type. Geomicrobiol J 25:149–156. https://doi.org/10.1080/01490450802006884.
56. Wrede C, Kokoschka S, Dreier A, Heller C, Reitner J, Hoppert M. 2013. Deposition of biogenic iron minerals in a methane oxidizing microbial mat. Archaea 2013:102972. https://doi.org/10.1155/2013/102972.
57. Wrede C, Krukenberg V, Dreier A, Reitner J, Heller C, Hoppert M. 2013. Detection of metabolic key enzymes of methane turnover processes in cold seep microbial biofilms. Geomicrobiol J 30:214–227. https://doi.org/10.1080/01490451.2012.665150.
58. Blakemore RP. 1982. Magnetotactic bacteria. Annu Rev Microbiol 36:217–238. https://doi.org/10.1146/annurev.mi.36.100182.001245.
59. Frankel RB. 1984. Magnetic guidance of organisms. Annu Rev Biophys Bioeng 13:85–103. https://doi.org/10.1146/annurev.bb.13.060184.000505.
60. Kopp RE, Kirschvink JL. 2008. The identification and biogeochemical

interpretation of fossil magnetotactic bacteria. Earth-Sci Rev 86:42–61. https://doi.org/10.1016/j.earscirev.2007.08.001.
61. Glasauer S, Langley S, Boyanov M, Lai B, Kemner K, Beveridge TJ. 2007. Mixed-valence cytoplasmic iron granules are linked to anaerobic respiration. Appl Environ Microbiol 73:993–996. https://doi.org/10.1128/AEM.01492-06.
62. Lovley DR. 2008. Extracellular electron transfer: wires, capacitors, iron lungs, and more. Geobiology 6:225–231. https://doi.org/10.1111/j.1472-4669.2008.00148.x.
63. Kremer A, Lippens S, Bartunkova S, Asselbergh B, Blanpain C, Fendrych M, Goossens A, Holt M, Janssens S, Krols M, Larsimont J-C, Mc Guire C, Nowack MK, Saelens X, Schertel A, Schepens B, Slezak M, Timmerman V, Theunis C, Van Brempt R, Visser Y, Guérin CJ. 2015. Developing 3D SEM in a broad biological context. J Microsc 259:80–96. https://doi.org/10.1111/jmi.12211.
64. Deerinck TJ, Shone TM, Bushong EA, Ramachandra R, Peltier ST, Ellisman MH. 1 December 2017. High-performance serial block-face SEM of nonconductive biological samples enabled by focal gas injection-based charge compensation. J Microsc https://doi.org/10.1111/jmi.12667.
65. Nauhaus K, Albrecht M, Elvert M, Boetius A, Widdel F. 2007. In vitro cell growth of marine archaeal-bacterial consortia during anaerobic oxidation of methane with sulfate. Environ Microbiol 9:187–196. https://doi.org/10.1111/j.1462-2920.2006.01127.x.
66. Alperin MJ, Hoehler TM. 2009. Anaerobic methane oxidation by archaea/sulfate-reducing bacteria aggregates. 1. Thermodynamic and physical constraints. Am J Sci 309:869–957.
67. Orcutt B, Meile C. 2008. Constraints on mechanisms and rates of anaerobic oxidation of methane by microbial consortia: process-based modeling of ANME-2 archaea and sulfate reducing bacteria interactions. Biogeosciences 5:1587–1599. https://doi.org/10.5194/bg-5-1587-2008.
68. Bratbak G. 1985. Bacterial biovolume and biomass estimations. Appl Environ Microbiol 49:1488–1493.
69. Lee S, Fuhrman JA. 1987. Relationships between biovolume and biomass of naturally derived marine bacterioplankton. Appl Environ Microbiol 53:1298–1303.
70. Musat N, Halm H, Winterholler B, Hoppe P, Peduzzi S, Hillion F, Horreard F, Amann R, Jørgensen BB, Kuypers MMM. 2008. A single-cell view on the ecophysiology of anaerobic phototrophic bacteria. Proc Natl Acad Sci U S A 105:17861–17866. https://doi.org/10.1073/pnas.0809329105.
71. Boutte CC, Henry JT, Crosson S. 2012. ppGpp and polyphosphate modulate cell cycle progression in Caulobacter crescentus. J Bacteriol 194:28–35. https://doi.org/10.1128/JB.05932-11.
72. Kuroda A, Nomura K, Ohtomo R, Kato J, Ikeda T, Takiguchi N, Ohtake H, Kornberg A. 2001. Role of inorganic polyphosphate in promoting ribosomal protein degradation by the Lon protease in *E. coli*. Science 293:705–708. https://doi.org/10.1126/science.1061315.
73. Racki LR, Tocheva EI, Dieterle MG, Sullivan MC, Jensen GJ, Newman DK. 2017. Polyphosphate granule biogenesis is temporally and functionally tied to cell cycle exit during starvation in Pseudomonas aeruginosa. Proc Natl Acad Sci U S A 114:E2440–E2449. https://doi.org/10.1073/pnas.1615575114.
74. Gérard E, Guyot F, Philippot P, López-García P. 2005. Fluorescence in situ hybridisation coupled to ultra small immunogold detection to identify prokaryotic cells using transmission and scanning electron microscopy. J Microbiol Methods 63:20–28. https://doi.org/10.1016/j.mimet.2005.02.018.
75. Halary S, Duperron S, Boudier T. 2011. Direct image-based correlative microscopy technique for coupling identification and structural investigation of bacterial symbionts associated with metazoans. Appl Environ Microbiol 77:4172–4179. https://doi.org/10.1128/AEM.02461-10.
76. Jahn MT, Markert SM, Ryu T, Ravasi T, Stigloher C, Hentschel U, Moitinho-Silva L. 2016. Shedding light on cell compartmentation in the candidate phylum Poribacteria by high resolution visualisation and transcriptional profiling. Sci Rep 6:35860. https://doi.org/10.1038/srep35860.
77. Knierim B, Luef B, Wilmes P, Webb RI, Auer M, Comolli LR, Banfield JF. 2012. Correlative microscopy for phylogenetic and ultrastructural characterization of microbial communities. Environ Microbiol Rep 4:36–41. https://doi.org/10.1111/j.1758-2229.2011.00275.x.
78. Milucka J, Widdel F, Shima S. 2013. Immunological detection of enzymes for sulfate reduction in anaerobic methane-oxidizing consortia. Environ Microbiol 15:1561–1571. https://doi.org/10.1111/1462-2920.12003.
79. Maki JS. 2013. Bacterial intracellular sulfur globules: structure and function. J Mol Microbiol Biotechnol 23:270–280. https://doi.org/10.1159/000351335.
80. Gorlas A, Marguet E, Gill S, Geslin C, Guigner J-M, Guyot F, Forterre P. 2015. Sulfur vesicles from Thermococcales: a possible role in sulfur detoxifying mechanisms. Biochimie 118:356–364. https://doi.org/10.1016/j.biochi.2015.07.026.
81. Gambelli L, Guerrero-Cruz S, Mesman RJ, Cremers G, Jetten MSM, den Camp HJMO, Kartal B, Lueke C, van Niftrik L. 2017. Community composition and ultrastructure of a nitrate-dependent anaerobic methane-oxidizing enrichment culture. Appl Environ Microbiol 84:e02186-17. https://doi.org/10.1128/AEM.02186-17.
82. Glöckner FO, Fuchs BM, Amann R. 1999. Bacterioplankton compositions of lakes and oceans: a first comparison based on fluorescence in situ hybridization. Appl Environ Microbiol 65:3721–3726.
83. Pernthaler J, Glöckner F-O, Schönhuber W, Amann R. 2001. Fluorescence in situ hybridization (FISH) with rRNA-targeted oligonucleotide probes, p 207–226. *In* Paul JH (ed), Methods in microbiology. Academic Press, Inc, San Diego, CA.
84. Stoecker K, Dorninger C, Daims H, Wagner M. 2010. Double labeling of oligonucleotide probes for fluorescence in situ hybridization (DOPE-FISH) improves signal intensity and increases rRNA accessibility. Appl Environ Microbiol 76:922–926. https://doi.org/10.1128/AEM.02456-09.
85. Humbel BM, de Jong MD, Müller WH, Verkleij AJ. 1998. Pre-embedding immunolabeling for electron microscopy: an evaluation of permeabilization methods and markers. Microsc Res Tech 42:43–58. https://doi.org/10.1002/(SICI)1097-0029(19980701)42:1<43::AID-JEMT6>3.0.CO;2-S.
86. Hunter RC, Hitchcock AP, Dynes JJ, Obst M, Beveridge TJ. 2008. Mapping the speciation of iron in Pseudomonas aeruginosa biofilms using scanning transmission X-ray microscopy. Environ Sci Technol 42:8766–8772. https://doi.org/10.1021/es801642z.
87. Deerinck T, Buschong E, Lev-Ram V, Shu X, Tsien R, Ellisman MH. 2010. Enhancing serial block-face scanning electron microscopy to enable high resolution 3-D nanohistology of cells and tissues. Microsc Microanal 16:1138–1139. https://doi.org/10.1017/S1431927610055170.
88. Gillies AR, Chapman MA, Bushong EA, Deerinck TJ, Ellisman MH, Lieber RL. 2017. High resolution three-dimensional reconstruction of fibrotic skeletal muscle extracellular matrix. J Physiol 595:1159–1171. https://doi.org/10.1113/JP273376.
89. Pernthaler A, Dekas AE, Brown CT, Goffredi SK, Embaye T, Orphan VJ. 2008. Diverse syntrophic partnerships from deep-sea methane vents revealed by direct cell capture and metagenomics. Proc Natl Acad Sci U S A 105:7052–7057. https://doi.org/10.1073/pnas.0711303105.
90. Kremer JR, Mastronarde DN, McIntosh JR. 1996. Computer visualization of three-dimensional image data using IMOD. J Struct Biol 116:71–76. https://doi.org/10.1006/jsbi.1996.0013.
91. Mastronarde DN. 1997. Dual-axis tomography: an approach with alignment methods that preserve resolution. J Struct Biol 120:343–352. https://doi.org/10.1006/jsbi.1997.3919.
92. Mastronarde DN, Held SR. 2017. Automated tilt series alignment and tomographic reconstruction in IMOD. J Struct Biol 197:102–113. https://doi.org/10.1016/j.jsb.2016.07.011.
93. R Core Development Team. 2013. R: a language and environment for statistical computing. R Foundation for Statistical Computing, Vienna, Austria.
94. RStudio, Inc. 2013. shiny: web application framework for R. R package, version 050.